



**HAL**  
open science

# Ocean Eddy Signature on SAR Derived Sea Ice Drift and Vorticity

Angelina Cassianides, Camille Lique, Anton Korosov

► **To cite this version:**

Angelina Cassianides, Camille Lique, Anton Korosov. Ocean Eddy Signature on SAR Derived Sea Ice Drift and Vorticity. *Geophysical Research Letters*, 2021, 48, 10.1029/2020GL092066 . insu-03683271

**HAL Id: insu-03683271**

**<https://insu.hal.science/insu-03683271>**

Submitted on 31 May 2022

**HAL** is a multi-disciplinary open access archive for the deposit and dissemination of scientific research documents, whether they are published or not. The documents may come from teaching and research institutions in France or abroad, or from public or private research centers.

L'archive ouverte pluridisciplinaire **HAL**, est destinée au dépôt et à la diffusion de documents scientifiques de niveau recherche, publiés ou non, émanant des établissements d'enseignement et de recherche français ou étrangers, des laboratoires publics ou privés.

Copyright

# Geophysical Research Letters

## RESEARCH LETTER

10.1029/2020GL092066

### Key Points:

- We develop a new method to identify under-ice ocean surface eddy in the Arctic from ice vorticity based on synthetic-aperture radar images
- We detect the signature of an eddy dipole with a horizontal scale of 80–100 km, persistent on a week, which was also sampled by a mooring

### Correspondence to:

A. Cassianides,  
[angelina.cassianides@ifremer.fr](mailto:angelina.cassianides@ifremer.fr)

### Citation:

Cassianides, A., Lique, C., & Korosov, A. (2021). Ocean eddy signature on SAR-derived sea ice drift and vorticity. *Geophysical Research Letters*, *48*, e2020GL092066. <https://doi.org/10.1029/2020GL092066>

Received 7 SEP 2020  
Accepted 11 FEB 2021

## Ocean Eddy Signature on SAR-Derived Sea Ice Drift and Vorticity

Angelina Cassianides<sup>1</sup> , Camille Lique<sup>1</sup> , and Anton Korosov<sup>2</sup> 

<sup>1</sup>Univ. Brest, CNRS, IRD, Ifremer, Laboratoire d'Océanographie Physique et Spatiale (LOPS), IUEM, Brest, France,  
<sup>2</sup>Nansen Environmental and Remote Sensing Center, Bergen, Norway

**Abstract** In the Arctic Ocean, the observation of mesoscale eddies is impeded by the presence of sea ice. To address this problem, we develop a new method of ocean eddy detection based on their signature in sea ice vorticity retrieved from synthetic-aperture radar (SAR) images. We examine the case of one eddy in October 2017 in the marginal ice zone of the Canadian Basin, which was sampled by mooring observations. Although the eddy could not be identified by visual inspection of the SAR images, its signature is revealed as a dipole anomaly in sea ice vorticity, which suggests that the eddy is a dipole composed of a cyclone and an anticyclone, with a horizontal scale of 80–100 km and persisted over a week. The robustness of our method will allow us to detect more eddies as more SAR observations become available in the future.

**Plain Language Summary** Mesoscale eddies are routinely observed by satellites in the ocean. Yet, in the ice-covered Arctic Basin, the presence of sea ice makes it challenging to characterize the eddy field. Here, we present a detection method of surface ocean eddies based on their signature in the displacement of sea ice, using high spatial resolution satellite images. A dipole composed of a cyclonic and an anticyclonic eddy is identified over a week in mid-October 2017 with a horizontal scale of 80–100 km. Its presence is confirmed by high values of ocean speed in the surface layer during the same period. This work demonstrates that processing is required for identifying the signature of eddies in sea ice, which is not always obvious at first sight.

### 1. Introduction

For decades, many studies have reported on the presence of mesoscale eddies in the ice-covered Arctic, randomly captured by in situ measurements (e.g., Manley & Hunkins, 1985; Newton et al., 1974). Recently, observations of high temporal and spatial resolution temperature and salinity profiles from Ice-Tethered Profilers (ITP; Toole et al., 2011) and moorings have allowed for the first time a census of the eddy characteristics (Carpenter & Timmermans, 2012; Zhao et al., 2014, 2016), revealing the presence of numerous small scale eddies at all depths in the Arctic interior, with horizontal length scales ranging from 5 to 20 km. Yet, the sampling of the Arctic Ocean by ITPs remains uneven, preventing us from obtaining a full description of the mesoscale activity at a Pan-Arctic scale. Moreover, in the ice-covered regions, satellites primarily return observations of the sea ice conditions, which do not allow for the usual identification of eddies based on the detection of their signature on surface properties (anomaly of sea level, temperature or tracers). Satellite-based detection of eddies is thus restricted to the ice-free regions of the Arctic and the marginal ice zone (MIZ).

There is growing evidence in the literature that the Arctic mesoscale activity and the sea ice might mutually influence each other. Aerial surveys (Johannessen et al., 1987) or high resolution satellite observations (Kozlov et al., 2019) of the Arctic MIZ have revealed swirling movements of sea ice that are the signature of ocean eddies. An example is shown in Figure 1a for October 2018 in the MIZ of the Canadian Basin. Using an idealized process model representing the MIZ, Manucharyan and Thompson (2017) have rationalized the imprint of (sub-)mesoscale eddies on sea ice, suggesting that, in the MIZ, sea ice tends to be trapped and accumulated in surface cyclonic eddies. Sea ice transported by eddies can locally affect the sea ice drift, producing strong sea ice deformation (Zhang et al., 1999). So far, the eddy detection in the MIZ was mostly based on visual inspection of satellite images (e.g., Kozlov et al., 2019), and may have missed a significant number of eddies when their signature is not directly recognizable. This method of detection is also based

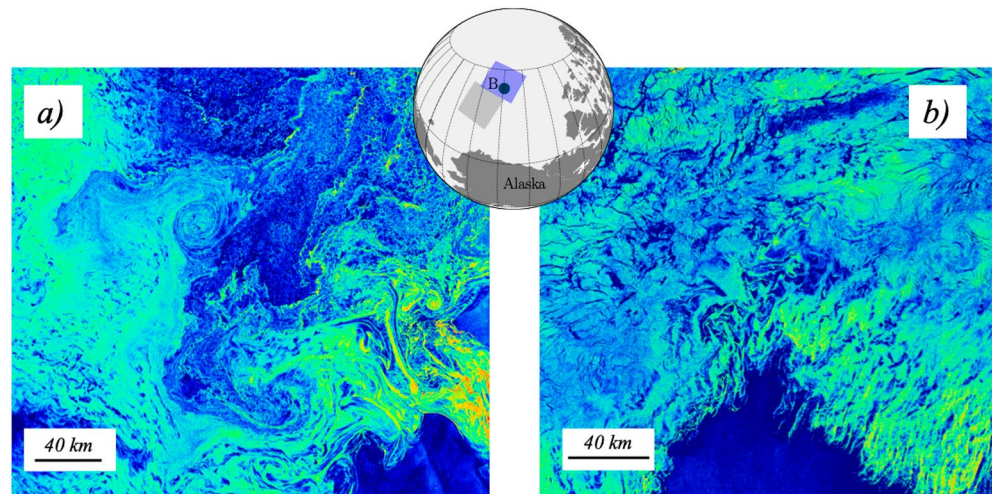


**Figure 1.** Examples of synthetic-aperture radar (SAR) images in the marginal ice zone (MIZ) of the Canadian Basin for (a) October 19, 2018 (centered around 76°N, 160°W) and (b) October 9, 2017 (centered around 78°N, 150°W). The inset map indicates the position of the two images (gray shading for (a) and purple for (b)), and the green dot is the position of mooring B. Colors visualize the SAR backscatter, with dark blue indicating ocean and green and yellow the presence of sea ice.

on the overly strong assumption that the signature of one eddy on sea ice would mimic exactly the shape and scale of the ocean feature itself, which is likely not the case in many instances (Gupta et al., 2020).

The goal of this paper is to present a new method to detect the signature of ocean surface eddies in sea ice vorticity, based on the analysis of high resolution images from synthetic-aperture radar (SAR). Here we mostly focus on one case study shown in Figure 1b, located in a MIZ of the Canadian Basin (around 78°N-150°W) in October 2017. This case is chosen as both sea ice and ocean observations are available at that time and location. Although no eddy imprint can be seen at first sight, we will show how further processing of the SAR images can reveal the presence of an ocean eddy. This paper is structured as follows. Section 2 briefly presents the data sets analyzed in this study. In Section 3, an ocean eddy is detected from mooring observations. The processing of SAR images and the eddy signature in sea ice vorticity are presented in Section 4. The robustness of the method is discussed in Section 5 and conclusions are given in Section 6.

## 2. Data

The primary in situ data used in this study are mooring observations from the Beaufort Gyre Exploration Project (BGEP; <https://www.whoj.edu>, Proshutinsky et al., 2009). Four moorings are deployed over the Beaufort Gyre since 2003. Upward-looking acoustic Doppler current profilers (ADCPs) are installed on the top of each mooring, returning profiles of ocean horizontal currents in the top ~30 m of the water column, with a resolution of 1 h and 2 m. Additionally, upward looking sonars (ULSs) are installed on the same moorings and provide a time series of ice draft with uncertainty of 5–10 cm (Krishfield & Proshutinsky, 2006). In the following, we use data from mooring B located at 78°N-150°W during 2017.

The sea ice response to the presence of mesoscale eddies is investigated using SAR imagery. The Sentinel-1 imaging radar mission, led by the European Space Agency (ESA), includes two satellites equipped with C-band SAR sensors: Sentinel-1A and Sentinel-1B launched in 2014 and 2016, respectively. The data product used here is the Level-1 Extra-Wide Swath mode ground range detected with medium resolution, available at the Copernicus Open Access Hub ([scihub.copernicus.eu](https://scihub.copernicus.eu)). The swath width is 400 km and the pixels are spaced by 40 × 40 m. HH (horizontal emission, horizontal receive) and HV (horizontal emission, vertical receive) polarization modes are used separately. The temporal resolution over the mooring location is uneven and depends on various factors such as the satellite's orbit or the acquisition mode. Hence, the time interval between two images varies from a few hours to a few days.

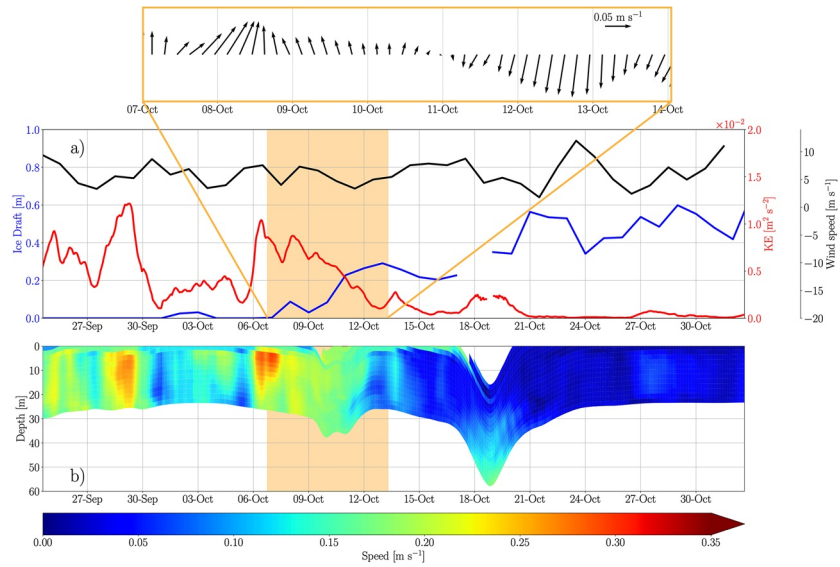


**Figure 2.** (a) Time series of ice draft (blue), KE (0–30 m, red) from the Acoustic Doppler Current Profiler (ADCP) and wind speed (black) in 2017. A stick diagram of the ocean current anomalies (relative to the mean over October 7–13) is shown in the orange box. (b) Ocean speed profiles from the ADCP.

We also make use of the Polar Pathfinder Sea Ice Motion Vectors version 4 from the National Snow and Ice Center (NSIDC, <https://nsidc.org>), which provides daily sea ice drift at the pan-Arctic scale with a resolution of 25 km over 1978 to 2019 (Tschudi et al., 2019). The error variance associated tends to be particularly large in the MIZ (Tschudi et al., 2020).

Finally, we estimate wind speed using the hourly averaged  $u_w$  and  $v_w$  wind speed at 10 m ( $U_{10} = \sqrt{(u_w^2 + v_w^2)}$ ) from the ERA5 reanalysis data with a spatial resolution of  $\sim 0.25^\circ$  (provided by ECMWF; Hersbach et al., 2020).

### 3. Ocean Eddy Detection from Mooring Observations

The first step of this study consists of the detection of an ocean eddy under sea ice. Zhao and Timmermans (2015) have shown that mesoscale eddies contribute to most of the kinetic energy sampled by the BGEP moorings below 60 m. Here, we follow the same method and apply it to the surface layer to identify an eddy passing by the mooring location by a large anomaly of kinetic energy. Using velocity measurements from mooring B's ADCP, we compute a time series of the depth-integrated kinetic energy (KE, normalized by the thickness of the surface layer  $h$ ) as:

$$KE = \int \left( \frac{1}{2} (u_o^2 + v_o^2) dz \right) / h \quad (1)$$

with  $u_o$  and  $v_o$  the ocean horizontal velocity components. Note that we have first filtered the high frequency fluctuations (likely induced by the inertial motion) in ocean velocity by applying a moving average with a 12 h moving window, as we are only interested in events that last over a few days.

Figure 2 displays time series of sea ice draft, KE integrated from 0 to  $\sim 30$  m depth and wind speed during September and October 2017, as well as the ocean speed profiles at mooring B. Before October 7, there is no sea ice at the mooring location (the sea ice draft is zero). High values of KE (close to  $1.3 \times 10^{-2} \text{ m}^2 \cdot \text{s}^{-2}$ ) are observed on two instances on September 28 and October 7. These two periods of high KE are related to increases in ocean speed from 0.15 to 0.3  $\text{m} \cdot \text{s}^{-1}$  (Figure 2b). After October 7, the sea ice draft increases drastically from 0 to more than 0.6 m while the KE decreases largely. The background flow under sea ice is weak, with mean velocities of 0.05  $\text{m} \cdot \text{s}^{-1}$  directed northward. After October 16, KE remains lower than  $0.5 \times 10^{-2} \text{ m}^2 \cdot \text{s}^{-2}$ . The time in between (October 7–13, the orange box) corresponds to the transition from

a period with high kinetic energy and no sea ice to a period with sea ice and very low kinetic energy on average. The anomaly in KE during that period suggests that the mooring is sampling an eddy passing by in the surface layer. The stick diagram of the ocean current anomalies (with respect to the mean over October 7–13; top inset in Figure 2) reveals a sign change, typical of the structure found in the core of an eddy. The ADCP data (and lack of associated density measurements) are not sufficient to allow a direct determination of the eddy's direction of rotation nor of its length scale. Using hydrographic data from CTD cast gathered during the deployment or recovery of the mooring, we estimate that the first deformation radius  $R_d$  in the interior of the Canadian Basin is on the order of  $\sim 13$  km, similar to the values suggested by Nurser and Bacon (2014) and Zhao et al. (2018). Following for instance Tulloch et al. (2011), this would imply that eddies generated by geostrophic turbulence would have a length scale around  $2\pi R_d \approx 82$  km.

Figure 2b also reveals two deep excursions of the ADCP on October 10 and 19, which are most likely the signature of eddies passing by the sub-surface layer, dragging the ADCP deeper (Krishfield & Proshutinsky, 2006). Note that the moorings are also equipped with a McLane Moored Profiler (MMP) that samples velocity, temperature and salinity profiles below 50 m. An examination of the MMP data confirms the presence of an anticyclonic eddy below the mixed-layer on October 18, with a core at 160 m depth (not shown). We are therefore in presence of two eddies propagating on top of each other under sea ice, with an anticyclone as the subsurface component. We hypothesize that these two eddies are the two parts of a dipole, as such features are frequently observed in the Arctic basin (Zhao et al., 2014). Indeed, results from idealized process models have suggested that dipoles are generated at surface front under sea ice (Brannigan et al., 2017), resulting in a cyclone in the surface layer on top of an anticyclone. In our case, it would mean that the surface part of the dipole sampled by the ADCP is a cyclone too.

It is worth noting that, during the full period considered here (September 25–October 30), wind speed remains relatively constant and weak at the mooring location, with an average of  $6 \text{ m}\cdot\text{s}^{-1}$  directed southwestward and no storm (Figure 2a). The lack of correlation between wind speed and kinetic energy suggests that the winds are not directly driving the evolution of the kinetic energy.

#### 4. Ocean Eddy Detection from Its Signature in Sea Ice Vorticity

Now that we have detected a pair of eddies from the mooring observations, the next step is to examine the sea ice conditions over that period. According to the OSISAF product (Tonboe et al., 2017, not shown), sea ice concentration at the mooring location is increasing rapidly as the sea ice starts freezing and the draft starts to increase after October 6, and reaches more than 50% from October 7 onward. Over October 7–13, eight SAR images covering the mooring position are available (one for the 7th, 8th, 9th, 10th, two for the 12th and 13th). Consecutive pairs of raw SAR images are first processed with the open-source software Nansat (Korosov et al., 2016). Sea ice drift is then estimated using an algorithm combining feature tracking and pattern matching techniques (Korosov & Rampal, 2017; Muckenhuber et al., 2016). The calculation is performed on a regular orthogonal grid of 4 km. The accuracy of this algorithm is below 300 m (Korosov & Rampal, 2017), resulting in an uncertainty of less than  $0.3 \text{ cm}\cdot\text{s}^{-1}$  for the sea ice drift. An example of a sea ice drift field for October 12–13 is presented in Figure 3a. The drift is directed westward and does not present a visible signature of swirling movement characteristic of the presence of mesoscale eddies.

We further compute the relative vorticity of sea ice, which presents the advantage of being a scalar, as:

$$\zeta_{ice} = \frac{\partial v_{ice}}{\partial x} - \frac{\partial u_{ice}}{\partial y} \quad (2)$$

with  $u_{ice}$  and  $v_{ice}$  the horizontal components of sea ice velocity. The sea ice vorticity estimated for October 12–13 is presented in Figure 3b. West of the mooring (green dot), there is a cyclonic signal (positive vorticity) with a horizontal scale of  $\sim 80$  km and values reaching more than  $2 \times 10^{-6} \text{ s}^{-1}$ . The background sea ice vorticity over most of the domain is negative (i.e., anticyclonic) with an intensity varying between  $-2 \times 10^{-7} \text{ s}^{-1}$  and  $-6 \times 10^{-6} \text{ s}^{-1}$ .

Ocean eddy are often identified through their strong anomaly in ocean vorticity. One would logically expect that an eddy advected under sea ice would exert a strong stress onto sea ice, possibly generating this way an

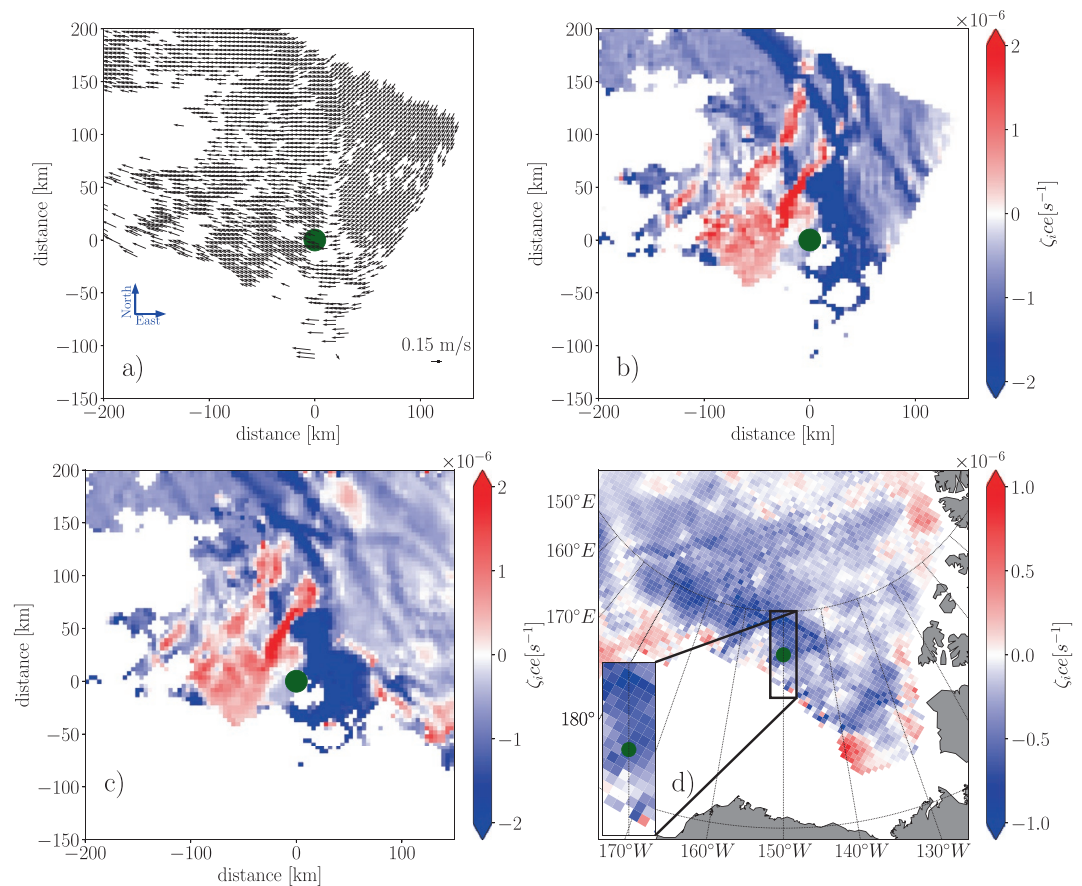


**Figure 3.** (a) Sea ice drift field and (b) sea ice vorticity from one pair of SAR images for October 12–13; (c) average of sea ice vorticity from five pairs of SAR images for October 7–13 and (d) from the National Snow and Ice Center (NSIDC) for October 7–13. The green dot indicates the position of mooring B, and the black box indicates the window of (a, b, and c).

anomaly in sea ice vorticity (Manucharyan & Thompson, 2017). Nonetheless, we do not expect fully similar ocean and sea ice vorticity fields, as both the wind forcing and the sea ice internal stress are also playing a role in the determination of the sea ice drift and vorticity (Hibler, 1979). In order to attribute the origin of anomaly in sea ice vorticity, we examine the different possible drivers. Our region of interest corresponds to the MIZ with low concentration and highly fractured sea ice, meaning that the rheology effects are relatively small. Over the period considered, there is no storm passing by the location of the mooring, while we have previously identified the presence of a surface eddy (Figure 2), suggesting that the eddy is most likely the primary driver of the sea ice vorticity signal.

Based on simple scaling arguments, we reinforce this attribution of the relative roles possibly played by the wind and the ocean eddy. First, the spatial scale of the cyclonic signal in sea ice vorticity ( $\sim 80$  km) is roughly similar to the expected length scale of the surface eddy. In contrast, atmospheric mesoscale features found in the Arctic have much larger characteristic scales. Polar lows (the most intense category of mesoscale atmospheric eddies), for instance, have scales ranging from 200 to 1,000 km (Terpstra et al., 2020; Wagner et al., 2011). Second, these storms have very short lifetime (typically a day or two). The availability of SAR images allows us to examine the persistence of the signal. Figure 3c shows the sea ice vorticity averaged over a week (October 7–13), estimated from all available SAR images (five pairs). The pattern is similar to the one obtained from any single pair of SAR images, although the intensity tends to be more pronounced when we average over a week (compare panels b and c of Figure 3). On average, two strong anomalies are visible close to the mooring: a cyclonic signal West of the mooring and an anticyclonic one East of it, both with

a horizontal scale of 80–100 km. Considering that our ocean dipole would be advected by the background flow with velocity of  $\sim 0.05 \text{ m}\cdot\text{s}^{-1}$ , it would have roughly travel northward by only 30 km over the week considered, consistent with the persistence of the sea ice vorticity pattern.

Finally, the intensity of the sea ice vorticity itself indicates that the ocean eddy is the most plausible driver. Following D'Asaro (1988) and Manley and Hunkins (1985), the ocean relative vorticity associated with a cyclonic eddy scales to  $\frac{2 \times U}{R}$ , with  $U$  the maximum azimuthal velocity of the eddy and  $R$  its radius. In the case of the cyclone sampled by mooring B,  $U$  is  $0.3 \text{ m}\cdot\text{s}^{-1}$ ,  $R$  is 41 km (corresponding to half the eddy length scale  $\frac{(2\pi R_d)}{2}$ ), resulting in a relative vorticity associated with the eddy of  $1.5 \times 10^{-5} \text{ s}^{-1}$ , larger than the intensity of the sea ice vorticity anomalies, which are around  $3 \times 10^{-6} \text{ s}^{-1}$  and  $-5 \times 10^{-6} \text{ s}^{-1}$  for the cyclone and the anticyclone, respectively. In order to estimate the order of magnitude of the sea ice vorticity driven by the wind, we compute the wind driven sea ice drift solely estimated from the wind, making use of the rule-of-thumb formulae of Thorndike and Colony (1982), that sea ice drifts at 2% of the wind speed with a direction of  $45^\circ$  to the right of the wind. Applying this computation to the ERA5 winds over the period considered (October 7–13), we obtain a widespread anticyclonic wind-driven ice vorticity over the region of the mooring, with a weak intensity of  $\sim -2 \times 10^{-7} \text{ s}^{-1}$  (not shown). This is an order of magnitude weaker than the strong sea ice vorticity detected by the SAR images, and a hundred time weaker than the vorticity found in the ocean eddy. It does, however, match well the intensity of the background sea ice vorticity (Figure 3c). More generally, the spatial pattern of the wind-driven sea ice vorticity matches closely the NSIDC vorticity, related to the large scale anticyclonic sea ice circulation within the wind-driven Beaufort gyre, suggesting that the NSIDC data set (with its resolution of 25 km and its large uncertainty of  $\pm 5 \text{ cm}\cdot\text{s}^{-1}$  for the period and region considered) is only able to capture the large scale wind driven drift, but not the smaller scale features driven by the ocean.

The combination of the sea ice vorticity anomaly and the presence of eddies captured by the mooring, the lack of a significant wind forcing over that period, and the scaling arguments presented before, allow us to attribute the signal to the signature of the ocean mesoscale eddies. The presence of two vorticity anomalies with opposite signs indicates that the signal is indeed a dipole, composed of a cyclone and an anticyclone.

## 5. Robustness of the Method

The analysis of our case study has revealed that the signature of the eddy (captured by the mooring observations) can be detected in the form of strong anomalies of sea ice vorticity over a few days. In order to ensure the robustness of our method, one must check that such anomalies in sea ice vorticity are not found in periods without ocean eddy detected by the mooring. As an example, we analyze a period of 4 days at the end of May 2018, during which 6 SAR images are available at the location of the mooring. Note that the low availability of Sentinel-1 SAR images largely limits the number of cases that can be examined. Between May 23–26, the sea ice draft fluctuates between 1.3 and 1.8 m and the KE remains very low, suggesting that no eddy is passing by during that period (Figure 4a). Applying the method described in the previous section, we estimate the sea ice drift for three pairs of SAR images and then the average ice vorticity (Figure 4b). The negative vorticity estimated from the SAR images matches well the amplitude of the vorticity estimated from the NSIDC sea ice drift, with values around  $-0.5 \times 10^{-6} \text{ s}^{-1}$  (Figure 4c). In contrast with the previous case, no local anomaly of ice vorticity is observed here, except for a localized positive anomaly whose shape suggests that is most likely the signature of a fracture in the ice pack. The results thus suggest that our method does not generate an eddy signature in sea ice vorticity when no eddy is captured in the surface layer, making us confident that our detection method is robust.

## 6. Conclusion

Mesoscale eddies are ubiquitous features in the Arctic Ocean but they are not easily observed from space because of the presence of sea ice. As a consequence, the detection of eddies has been limited to open water regions and MIZ. In this paper, a new methodology of ocean eddy detection has been presented, based on

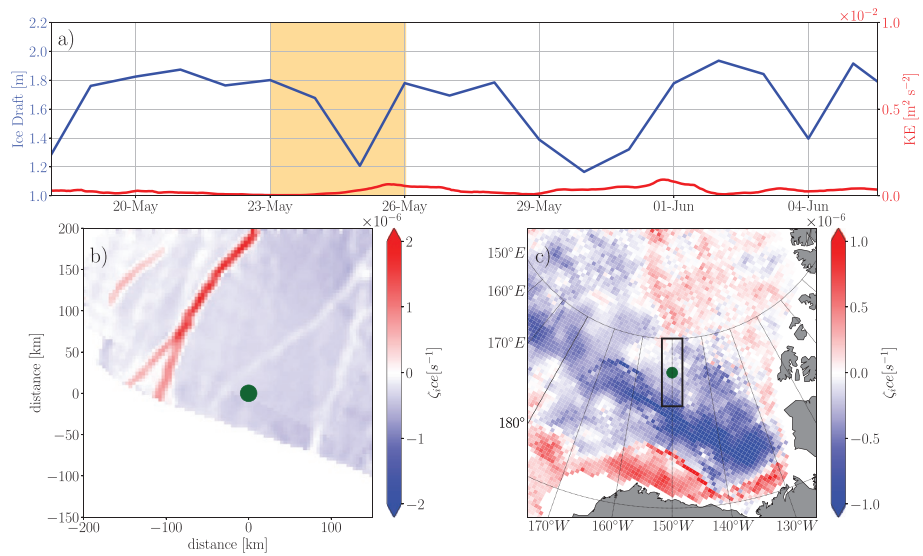


**Figure 4.** Time series of ice draft (blue) and KE (0–30 m, red) from the ADCP in 2018 (a). The orange box in (a) shows the period of interest between May 23–26. Average of sea ice vorticity from three pairs of SAR images (b) and from NSIDC (c) for May 23–26, 2018. The green dot is the position of the mooring and the black box in (c) indicates the window of (b).

the response of the sea ice drift to the passage of an ocean eddy. A case study is presented for October 2017 in the Canadian Basin: in situ data from one mooring have efficiently allowed us to detect eddies under sea ice in the MIZ. Pairs of SAR images are used to determine the sea ice drift and vorticity at a spatial resolution high enough to detect the signature of mesoscale features. The sea ice vorticity indeed reveals the presence of a dipole with two anomalies of different signs. These are the signatures of eddies detected by a mooring, which samples two anomalies that are likely a dipole composed of a cyclone and an anticyclone. We suggest that the method presented here could be efficiently used to perform semi-automatic detection of ocean eddy in the surface layer of the ice-covered Arctic, in the MIZ and beyond. The main limitation is the availability of data which severely constrains the number of cases that can be captured. However, as moorings and ITPs are routinely deployed in the Arctic and the spatiotemporal coverage of SAR satellites is improving, future data will be available for identifying other cases of eddy imprint. Sea ice conditions are also an important factor limiting the detection. In late spring and summer, the sea ice drift cannot be recovered from the algorithm used here as sea ice is largely fragmented or covered by numerous melt ponds. Conversely, in winter, thicker sea ice tends to dissipate surface eddies (Meneghello et al., 2020). As the sea ice pack transitions toward a thinner, more mobile pack, the dissipation exerted by sea ice on eddies will likely decrease, possibly modifying the nature of the Arctic mesoscale activity. Improving the observability of the Arctic eddy is a major challenge in order to better understand the functioning of the Arctic system and predict its evolution.

Further investigations should also focus on the mechanisms at play for the eddy signature on sea ice, in order to improve the method presented here. Anomalies of vorticity presented here suggest that the ocean dipole generates regions of strong sea ice deformation and divergence. Zhang et al. (1999) simulated such sea ice behaviors in the presence of ocean eddies, resulting in thinner and less compact ice and even in regions of open water when ice deformation becomes large, in which we expect intensified air-sea heat exchanges and sea ice melt. Besides, vertical heat fluxes located in cyclonic eddies could bring warm waters in the surface layer and contribute to sea ice melt (Manucharyan & Thompson, 2017). In addition to the dynamical effects, such thermodynamical mechanisms could modify the sea ice conditions and thus enhance the eddy signature (Gupta et al., 2020). All these possible interactions between mesoscale eddy and sea ice need to be better understood in order to explain the different signals found in satellite observations of sea ice.

### Data Availability Statement

The hydrographic data were collected and made available by the Beaufort Gyre Exploration Program based at the Woods Hole Oceanographic Institution (<http://www.whoi.edu/beaufortgyre>). The satellite data was provided by the European Space Agency and the National Snow and Ice Data Center. The wind reanalysis data are provided by the European Centre for Medium-Range Weather Forecasts.

### Acknowledgments

We acknowledge funding from the French ANR through the project Im-MEDIAT (Grant ANR-18-CE01-0010) as well as funding from Ifremer. The study was supported by Arktalas Hoavva project (no AO/1-9595/18/NL/LF) funded by European Space Agency.

### References

Brannigan, L., Johnson, H., Lique, C., Nycander, J., & Nilsson, J. (2017). Generation of subsurface anticyclones at Arctic surface fronts due to a surface stress. *Journal of Physical Oceanography*, 47(11), 2653–2671. <https://doi.org/10.1175/JPO-D-17-0022.1>

Carpenter, J. R., & Timmermans, M. (2012). Deep mesoscale eddies in the Canada Basin, Arctic Ocean. *Geophysical Research Letters*, 39(20). <https://doi.org/10.1029/2012GL053025>

D’Asaro, E. A. (1988). Observations of small eddies in the Beaufort Sea. *Journal of Geophysical Research*, 93(C6), 6669. <https://doi.org/10.1029/jc093ic06p06669>

Gupta, M., Marshall, J., Song, H., Campin, J., & Meneghello, G. (2020). Sea-ice melt driven by ice-ocean stresses on the mesoscale. *Journal of Geophysical Research: Oceans*, 125(11), e2020JC016404. <https://doi.org/10.1029/2020jc016404>

Hersbach, H., Bell, B., Berrisford, P., Hirahara, S., Horányi, A., Muñoz-Sabater, J., et al. (2020). The ERA5 global reanalysis. *Quarterly Journal of the Royal Meteorological Society*, 146(730), 1999–2049. <https://doi.org/10.1002/qj.3803>

Hibler, W. D. (1979). A dynamic thermodynamic sea ice model. *Journal of Physical Oceanography*, 9(4), 815–846. [https://doi.org/10.1175/1520-0485\(1979\)009<0815:adtsim>2.0.co;2](https://doi.org/10.1175/1520-0485(1979)009<0815:adtsim>2.0.co;2)

Johannessen, O. M., Johannessen, J. A., Svendsen, E., Shuchman, R. A., Campbell, W. J., & Josberger, E. (1987). Ice-edge eddies in the Fram Strait marginal ice zone. *Science*, 236(4800), 427–429. <https://doi.org/10.1126/science.236.4800.427>

Korosov, A., Hansen, M. W., Dagestad, K.-F., Yamakawa, A., Vines, A., & Riechert, M. (2016). Nansat: A scientist-orientated python package for geospatial data processing. *Journal of Open Research Software*, 4(1), 39. <https://doi.org/10.5334/jors.120>

Korosov, A., & Rampal, P. (2017). A combination of feature tracking and pattern matching with optimal parametrization for sea ice drift retrieval from SAR data. *Remote Sensing*, 9(3), 258. <https://doi.org/10.3390/rs9030258>

Kozlov, I. E., Artamonova, A. V., Manucharyan, G. E., & Kubryakov, A. A. (2019). Eddies in the Western Arctic Ocean from spaceborne SAR observations over open ocean and marginal ice zones. *Journal of Geophysical Research: Oceans*, 124(9), 6601–6616. <https://doi.org/10.1029/2019JC015113>

Krishfield, R., & Proshutinsky, A. (2006). *BGOS ULS data processing procedure* (Technical Report). Woods Hole Oceanographic Institution.

Manley, T. O., & Hunkins, K. (1985). Mesoscale eddies of the Arctic Ocean. *Journal of Geophysical Research*, 90(C3), 4911. <https://doi.org/10.1029/jc090ic03p04911>

Manucharyan, G. E., & Thompson, A. F. (2017). Submesoscale sea ice-ocean interactions in marginal ice zones. *Journal of Geophysical Research: Oceans*, 122(12), 9455–9475. <https://doi.org/10.1002/2017JC012895>

Meneghello, G., Marshall, J., Lique, C., Isachsen, P. E., Doddridge, E., Campin, J.-M., & Talandier, C. (2020). Genesis and decay of mesoscale baroclinic eddies in the seasonally ice-covered interior Arctic Ocean. *Journal of Physical Oceanography*, 51(1), 115–129. <https://doi.org/10.1175/JPO-D-20-0054.1>

Muckenhuber, S., Korosov, A., & Sandven, S. (2016). Open-source feature-tracking algorithm for sea ice drift retrieval from Sentinel-1 SAR imagery. *The Cryosphere*, 10(2), 913–925. <https://doi.org/10.5194/tc-10-913-2016>

Newton, J. L., Aagaard, K., & Coachman, L. K. (1974). Baroclinic eddies in the Arctic Ocean. *Deep Sea Research and Oceanographic Abstracts*, 21(9), 707–719. [https://doi.org/10.1016/0011-7471\(74\)90078-3](https://doi.org/10.1016/0011-7471(74)90078-3)

Nurser, A. J. G., & Bacon, S. (2014). The Rossby radius in the Arctic Ocean. *Ocean Science*, 10(6), 967–975. <https://doi.org/10.5194/os-10-967-2014>

Proshutinsky, A., Krishfield, R., Timmermans, M.-L., Toole, J., Carmack, E., McLaughlin, F., et al. (2009). Beaufort Gyre freshwater reservoir: State and variability from observations. *Journal of Geophysical Research*, 114(C1). <https://doi.org/10.1029/2008JC005104>

Terpstra, A., Watanabe, S.-I., Terpstra, A., & Watanabe, S.-I. (2020). Polar lows. In *Oxford research encyclopedia of climate science*. Oxford University Press. <https://doi.org/10.1093/acrefore/9780190228620.013.775>

Thorndike, A. S., & Colony, R. (1982). Sea ice motion in response to geostrophic winds. *Journal of Geophysical Research*, 87(C8), 5845. <https://doi.org/10.1029/jc087ic08p05845>

Tonboe, R., Lavelle, J., Pfeiffer, R.-H., & Howe, E. (2017). *Ocean & sea ice SAF product user manual for OSI SAF global sea ice concentration* (Technical Report). Danish Meteorological Institute.

Toole, J., Krishfield, R., Timmermans, M.-L., & Proshutinsky, A. (2011). The Ice-Tethered Profiler: Argo of the Arctic. *Oceanography*, 24(3), 126–135. <https://doi.org/10.5670/oceanog.2011.64>

Tschudi, M., Meier, W. N., & Stewart, J. S. (2020). An enhancement to sea ice motion and age products at the National Snow and Ice Data Center (NSIDC). *The Cryosphere*, 14(5), 1519–1536. <https://doi.org/10.5194/tc-14-1519-2020>

Tschudi, M., Meier, W. N., Stewart, J. S., Fowler, C., & Maslanik, J. (2019). *Polar Pathfinder Daily 25 km EASE-Grid Sea Ice Motion Vectors, version 4*. Boulder, CA, USA: National Snow and Ice Data Center. Retrieved from <https://doi.org/10.5067/INAWUW07QH7B>

Tulloch, R., Marshall, J., Hill, C., & Smith, K. S. (2011). Scales, growth rates, and spectral fluxes of baroclinic instability in the ocean. *Journal of Physical Oceanography*, 41(6), 1057–1076. <https://doi.org/10.1175/2011JPO4404.1>

Wagner, J. S., Gohm, A., Dörnbrack, A., & Schäfler, A. (2011). The mesoscale structure of a polar low: Airborne lidar measurements and simulations. *Quarterly Journal of the Royal Meteorological Society*, 137(659), 1516–1531. <https://doi.org/10.1002/qj.857>

Zhang, Y., Maslowski, W., & Semtner, A. J. (1999). Impact of mesoscale ocean currents on sea ice in high-resolution Arctic ice and ocean simulations. *Journal of Geophysical Research: Oceans*, 104(C8), 18409–18429. <https://doi.org/10.1029/1999jc900158>

Zhao, M., & Timmermans, M. (2015). Vertical scales and dynamics of eddies in the Arctic Ocean’s Canada Basin. *Journal of Geophysical Research: Oceans*, 120(12), 8195–8209. <https://doi.org/10.1002/2015JC011251>

Zhao, M., Timmermans, M., Krishfield, R., & Manucharyan, G. (2018). Partitioning of kinetic energy in the Arctic Ocean’s Beaufort Gyre. *Journal of Geophysical Research: Oceans*, 123(7), 4806–4819. <https://doi.org/10.1029/2018JC014037>

- Zhao, M., Timmermans, M.-L., Cole, S., Krishfield, R., Proshutinsky, A., & Toole, J. (2014). Characterizing the eddy field in the Arctic Ocean halocline. *Journal of Geophysical Research: Oceans*, *119*(12), 8800–8817. <https://doi.org/10.1002/2014JC010488>
- Zhao, M., Timmermans, M.-L., Cole, S., Krishfield, R., & Toole, J. (2016). Evolution of the eddy field in the Arctic Ocean's Canada Basin, 2005–2015. *Geophysical Research Letters*, *43*(15), 8106–8114. <https://doi.org/10.1002/2016GL069671>